Twist engineering of the two-dimensional magnetism in double bilayer chromium triiodide homostructures

Hongchao Xie
University of Michigan https://orcid.org/0000-0001-8525-9852
Xiangpeng Luo
University of Michigan
Gaihua Ye
Texas Tech University
Zhipeng Ye
Texas Tech University
Haiwen Ge
Texas Tech University
Suk Hyun Sung
University of Michigan-Ann Arbor https://orcid.org/0000-0002-7491-1988
Emily Rennich
University of Michigan
Shaohua Yan
Renmin University of China
Yang Fu
Renmin University of China
Shang-Jie Tian
Renmin University of China https://orcid.org/0000-0002-3412-4656
Hechang Lei
Renmin University of China https://orcid.org/0000-0003-0850-8514
Robert Hovden
University of Michigan https://orcid.org/0000-0002-3403-8803
Kai Sun
University of Michigan–Ann Arbor https://orcid.org/0000-0001-9595-7646
Rui He
Texas Tech University https://orcid.org/0000-0002-2368-7269
Liuyan Zhao (lyzhao@umich.edu)
University of Michigan-Ann Arbor https://orcid.org/0000-0001-9512-3537

Letter

Keywords: twist engineering, two-dimensional (2D) crystalline layers, 2D science, magnetism

Posted Date: March 25th, 2021

DOI: https://doi.org/10.21203/rs.3.rs-356604/v1

Version of Record: A version of this preprint was published at Nature Physics on December 2nd, 2021.
See the published version at https://doi.org/10.1038/s41567-021-01408-8.

Twist engineering of the two-dimensional magnetism in double bilayer chromium triiodide homostructures

Hongchao Xie[1,+], Xiangpeng Luo[1,+], Gaihua Ye[2,+], Zhipeng Ye[2], Haiwen Ge[3], Suk Hyun Sung[4], Emily Rennich[5], Shaohua Yan[6], Yang Fu[6], Shangjie Tian[6], Hechang Lei[6], Robert Hovden[4], Kai Sun[1], Rui He[2,*], & Liuyan Zhao[1,*]

[1] Department of Physics, University of Michigan, 450 Church Street, Ann Arbor, MI, 48109, USA
[2] Department of Electrical and Computer Engineering, Texas Tech University, 910 Boston Avenue, Lubbock, TX, 79409, USA
[3] Department of Mechanical Engineering, Texas Tech University, 2703 7th Street, Lubbock, TX 79409, USA
[4] Department of Materials Science and Engineering, University of Michigan, 2300 Hayward Street, Ann Arbor, MI, 48109, USA
[5] Department of Mechanical Engineering, University of Michigan, 2350 Hayward Street, Ann Arbor, MI, 48109, USA
[6] Department of Physics and Beijing Key Laboratory of Opto-electronic Functional Materials & Micro-Nano Devices, Renmin University of China, Beijing, 100872, China

[*] Email: rui.he@ttu.edu; lyzhao@umich.edu
[+] These authors contributed equally

Twist engineering, or the alignment of two-dimensional (2D) crystalline layers with desired orientations, has led to tremendous success in modulating the charge degree of freedom in hetero- and homo-structures, in particular, in achieving novel correlated and topological electronic phases in moiré electronic crystals [1,2]. However, although pioneering theoretical efforts have predicted nontrivial magnetism [3,4] and magnons [5] out of twisting 2D magnets, experimental realization of twist engineering spin degree of freedom remains elusive. Here, we leverage the archetypal 2D Ising magnet chromium triiodide (CrI_3) to fabricate twisted double bilayer homostructures with tunable twist angles and demonstrate the successful twist engineering of 2D magnetism in them. Using linear and circular polarization-resolved Raman spectroscopy, we identify magneto-Raman signatures of a new magnetic ground state that is sharply distinct from those in natural bilayer (2L) and four-layer (4L) CrI_3. With careful magnetic field and twist angle dependence, we reveal that, for a very small twist angle (~ 0.5°), this emergent magnetism can be well-approximated by a weighted linear superposition of those of 2L and 4L CI_3 whereas, for a relatively large twist angle (~ 5°), it mostly resembles that of isolated 2L CrI_3. Remarkably, at an intermediate twist angle (~ 1.1°), its magnetism cannot be simply inferred from the 2L and 4L cases, because it lacks sharp spin-flip transitions that are present in 2L and 4L CrI_3 and features a dramatic Raman circular dichroism that is absent in natural 2L and 4L ones. Our results demonstrate the possibility of designing and controlling the spin degree of freedom in 2D magnets using twist engineering.

Moiré superlattice forms when two vertically stacked atomic crystals are rotated with respect to each other, enabling a powerful venue to design and tailor the physical properties of 2D materials, including electronic, phononic, and magnetic ones. So far, it has achieved fruitful results in controlling the charge degree of freedom (DoF) and realizing novel quantum phenomena in both single-particle electronic states and two-particle excitonic states. Outstanding examples include the creation of flat electronic bands [1,2] that leads to various strongly correlated [6-10] and topological [11-13] phases for the former case, and the introduction of deep confinement potential that localizes excitonic states to realize moiré excitons [14,15], exciton Mott insulators [16], and quantum emitters [17] for the latter. Recently, it has also shown significant impacts on modulating the lattice DoF and induced lattice reconstructions [18,19], renormalized phonons [20], and moiré phonons [21]. In sharp contrast, the potential and power of moiré superlattices in controlling the spin DoF and engineering the magnetic properties have remained as a pristine area experimentally, despite a few pioneering theoretical predictions including noncollinear magnetism [3], topological magnetism [4], moiré magnon bands [5], and one-dimensional magnons [5].

Newly discovered layered magnets have greatly expanded the library of two-dimensional (2D) materials and provided exciting possibilities for the exploration and exploitation of the intrinsic spin DoF at the atomically thin limit [22-24]. Among the 2D magnetic atomic crystals discovered thus far, atomically thin chromium trihalides, CrX_3 (X = Cl, Br, and I) have attracted extensive interest as an archetype 2D magnet platform for hosting a plethora of novel 2D magnetic phenomena [25-31] and exhibiting versatile tunability with external stimuli [32-36]. In particular, it has been theoretically calculated [37] and experimentally shown [35,36] in bilayer (2L) CrI_3 that tuning between the monoclinic (AB') and rhombohedral (AB) stacking geometries can lead to magnetic transitions from the layered antiferromagnetic (AFM) to ferromagnetic (FM) order. Such a close relationship between structural stacking symmetries and interlayer magnetism in CrI_3 naturally stimulates the curiosity of investigating the magnetism in CrI_3 moiré magnets where the interlayer exchange coupling is periodically modulated in both sign (i.e., AFM vs FM) and strength (i.e., magnitude).

Here, we fabricate twisted double bilayer (tDB) CrI_3 homostructures with individual 2L CrI_3 to engineer the inter-2L exchange coupling and investigate the resulting moiré magnetism. Our choice of 2L CrI_3 as the building block is based on its significantly narrower structural and magnetic phonon linewidths than those of monolayer CrI_3, suggesting a much better crystalline and magnetic integrity in 2L CrI_3 [38,39]. Figure 1a top panel shows a false-color optical image of a typical tDB CrI_3 sample that was made by tearing a large piece of 2L CrI_3 in the bottom panel into two and then stacking them together at a controlled twist angle of α (see Methods). Electron diffraction (Fig. 1b) shows two sets of 1st and 2nd order Bragg peaks for the two 2L CrI_3 in a tDB CrI_3 sample with the targeted α of 1.0° during fabrication, from which the actual α was

determined to be 0.9° on average with a standard deviation of 0.1° through surveying nine different locations on this sample. The match between targeted and measured values confirms our well control of the twist angle in fabrications, and the small standard deviation suggests the homogeneity of our samples. Dark field transmission electron microscopy (TEM) (Fig. 1c) displays the real-space periodic superstructures with noticeable domain formation. The bright triangles are associated with the strongly coupled regions between two 2L CrI_3 whereas the dark boundaries represent the decoupled boundaries. Similar reconstructuring has been observed in low-twist angle graphene bilayers[19] and transition metal dichalcogenide bilayers [18].

Magneto-Raman spectroscopy can capture the interlayer magnetism in few-layer CrI_3, by detecting the unique static magnetism-coupled phonons that break the time-reversal symmetry and have antisymmetric Raman tensors [38-42], in addition to the conventional pure structural phonons. Figure 1d presents representative Raman spectra of tDB CrI_3 with the targeted α = 1.1° in both the crossed and parallel linear polarization channels at 10 K, featuring key Raman modes in three spectral ranges, 75 to 85 cm^{-1}, 95 to 120 cm^{-1}, and 120 to 133 cm^{-1}. These modes are coarsely comparable to those of few-layer CrI_3 among which the Raman modes in the 75 to 85 cm^{-1} and 120 to 140 cm^{-1} ranges particularly highlight the contribution from the magnetism-coupled-phonon scattering [38]. In this work, we focus on the 120 to 133 cm^{-1} range because the Raman modes here could be related to the moiré magnetism and are of higher intensity than those in 75 to 85 cm^{-1}. Figure 1e zooms into the Raman spectra in the 120 to 133 cm^{-1} range and includes data in both linearly crossed and parallel channels with incident polarizations at the horizontal and 45° rotated directions, i.e., θ_{inc} = 0° and 45°. Clearly, the one primary mode in the parallel channels (U_1^t at 129.4 cm^{-1}) and the three modes in the crossed channels ($U_{2,3,4}^t$ at 129.0 cm^{-1}, 127.4 cm^{-1}, and 126.3 cm^{-1}) all and individually show no polarization dependence, confirming that Raman modes in the crossed (parallel) channels correspond to antisymmetric (fully symmetric) Raman tensors, thus break (preserve) the time-reversal symmetry, and correspond to the static magnetism-coupled (pure structural) phonon contribution, similar to those in natural few-layer CrI_3 [38]. On the other hand, the triplet lineshape of the tDB CrI_3 Raman spectra in the crossed channel shows a clear distinction from those of 2L and 4L CrI_3 with a single (U_2^{2L} at 127.1 cm^{-1}) and two (U_2^{4L} at 128.6 cm^{-1} and U_4^{4L} at 125.7 cm^{-1}) Raman modes, respectively [38], shown in Fig. 2a. Such a distinction strongly suggests the substantial difference in the magnetism between tDB CrI_3 and natural 2L/4L CrI_3.

Having established the Raman signature for the magnetism of tDB CrI_3 and its distinction from those of natural 2L/ 4L CrI_3, we proceed to examine its twist angle dependence. Figure 2a collects Raman spectra over 120 – 133 cm^{-1} taken on tDB CrI_3 of selected α = 0.5°, 1.1°, 2.0°, and 5.0°, as well as 4L and 2L CrI_3, in both the crossed and parallel linear polarization channels at 10 K. We observe that the central mode (U_3^t) in the triplet in the crossed channel increases in intensity and the two modes on its side ($U_{2,4}^t$) decrease as

the twist angle α increases, showing the trend that the magneto-Raman spectra of tDB CrI_3 evolves from resembling most the natural 4L CrI_3 at the lowest α to converging towards the 2L CrI_3 at the highest α. This trend is expected because the inter-2L coupling strength in tDB CrI_3 weakens at larger α, leading to the parallel stacked ($\alpha = 0^o$) tDB CrI_3 relaxing to a 4L CrI_3 flake and the large twist angle ones are equivalent to two decoupled 2L CrI_3 films. This intensity evolution is further quantitatively summarized in Fig. 2c where the relative intensity ratio $I_{U_3^t}/(I_{U_2^t} + I_{U_4^t})$ is plotted against α for tDB CrI_3 and compared with those of 4L and 2L CrI_3, showing a monotonous enhancement with increasing α and further confirming the corresponding reduction of inter-2L coupling at larger α. Equally informative is the frequency shift of the Raman modes which is shown in Fig. 2b. At low twist angles (*e.g.*, α = 0.5°, 1.1°), the frequencies of U_2^t and U_4^t in tDB CrI_3 match with those of U_2^{4L} and U_4^{4L} in 4L CrI_3, respectively, whereas the frequency of U_3^t is close to that of U_2^{2L} in 2L CrI_3 which appears in the crossed channel same as U_3^t does and that of U_3^{4L} in 4L CrI_3 which is however absent in the crossed channel in contrast to U_3^t. As the twist angle increases, the frequencies of U_2^t and U_4^t blueshift towards their high-frequency neighbors U_1^t and U_3^t. Eventually, at large twist angles (*e.g.*, α = 5°), the frequencies of $U_{2,4}^t$ become nearly indistinguishable from $U_{1,3}^t$ and approaches those of $U_{1,2}^{2L}$ in 2L CrI_3. The correspondence of mode frequencies between the fabricated tDB CrI_3 and the natural 4L/2L CrI_3 reveals that magnetism-coupled-phonon contributions for U_2^t and U_4^t arise from regions with strong inter-2L coupling, resembling the 4L-like case, whereas that for U_3^t is dominated by the decoupled regions, mimicking the 2L-like case. The twist angle dependencies of mode frequencies and the relative intensity ratio both confirm the reduction of inter-2L coupling and the suppression of strongly coupled 2L-2L regions in tDB CrI_3 at larger α.

Out-of-plane magnetic field ($B_\perp$) is known to introduce sharp spin-flip transitions in few-layer CrI_3, which is nicely captured in the $B_\perp$ dependence of Raman spectra of the magnetism-coupled phonon scattering [38]. We now proceed to more in-depth investigations of the engineered magnetism in tDB CrI_3 by performing its magnetic field dependencies for selected twist angles and comparing them across one another and with natural 4L/2L CrI_3. Figures 3a-e present the false color maps of the $B_\perp$ dependent magneto-Raman spectra for 4L CrI_3, tDB CrI_3 at selected twist angles of α = 0.5°, 1.1°, and 5.0°, and 2L CrI_3, respectively, in the linearly crossed channel at 10 K, and Figures 3f-j summarize their corresponding $B_\perp$ dependencies of the fitted mode intensities of the magnetism-coupled phonons. We first briefly summarize the evolutions of $U_i^{4L/2L}$, with i = 1 – 4 for 4L and i = 1 – 2 for 2L CrI_3, upon increasing $B_\perp$ as a reference for understanding those of U_{1-4}^t for tDB CrI_3. For 4L CrI_3, U_1^{4L} and U_3^{4L} emerge abruptly at B_{c1} = 0.7 T and then sharply jump upwards and downwards, respectively, at B_{c2} = 1.6 T, whereas U_2^{4L} and U_4^{4L} both experience two consecutive steep drops at B_{c1} and B_{c2}, with plateaus of constant intensities outside of B_{c1}

and B_{c2}, for which B_{c1} and B_{c2} correspond to two first-order spin flip transitions for the layered magnetism transiting from ↑↓↑↓ (layered AFM) first to ↑↓↑↑ and then to ↑↑↑↑ (fully polarized FM), respectively [25], with ↑ (↓) for out-of-plane magnetic moment aligning up (down). For 2L CrI_3, U_1^{2L} appears and U_2^{2L} disappears concurrently at B_c = 0.7 T with B_c for the spin flip transition from ↑↓ to ↑↑ [25].

We now turn to the magnetic field dependencies of U_{1-4}^t in tDB CrI_3 at very small (α = 0.5°) and relatively large (α = 5°) twist angles, both of which can be well described by a simple weighted linear superposition of those of 4L and 2L CrI_3. Similar to the 4L case (Figs. 3a and 3f), the 0.5° tDB CrI_3 features two transitions at B_{c1} = 0.7 T and B_{c2} = 1.6 T with jumps/drops in U_{1-4}^t mode intensities near B_{c1} and B_{c2} of the same trends as those in 4L CrI_3 and plateaus of constant intensities otherwise (Figs. 3b and 3g). Different from the 4L case, U_3^t of the 0.5° tDB CrI_3 is present even below B_{c1}, and the transitions are slightly broadened. As discussed in Fig. 2, U_2^t and U_4^t only originate from regions with strong coupling between the two bilayers in tDB CrI_3, whereas U_1^t and U_3^t match in frequency with modes in both coupled and decoupled regions. Thus, the behaviors of U_{1-4}^t in the 0.5° tDB CrI_3 can be well accounted for by a weighted add-up of the $B_\perp$ dependencies of U_{1-4}^{4L} and U_{1-2}^{2L} that correspond to the contributions from the strongly coupled and the decoupled 2L-2L regions, respectively. On the other hand, the 5.0° tDB CrI_3 in Figs. 3d and 3i nearly replicates the 2L CrI_3 results in Figs. 3e and 3j, except a minor remnant in U_3^t above B_c = 0.7 T. This observation confirms that the 5.0° tDB CrI_3 is primarily regarded as two decoupled 2L CrI_3 with only a tiny fraction of coupled regions. Therefore, the magnetism for both the 0.5° and 5.0° tDB CrI_3 can be well described by the combinations of those of 4L and 2L CrI_3, which makes sense because at very low twist angles (*e.g.*, 0.5°), the structure of tDB CrI_3 relaxes to maximize the natural 4L-like regions whereas at large twist angles (*e.g.*, 5.0°), the inter-2L coupling in tDB CrI_3 is so significantly reduced to approach two decoupled 2L CrI_3, similar to many other van der Waals homo- and hetero-structures.

Interestingly, in stark contrast to the 0.5° and 5.0° tDB CrI_3, the magnetism in the 1.1° tDB CrI_3 can no longer be understood simply from the combination of 4L and 2L CrI_3 because its $B_\perp$ dependence features two key behaviors that are not at all present in those of 4L and 2L CrI_3 (Figs. 3c and 3h). First, around B_{c1} ≈ 0.6 T, the intensities of U_2^t and U_4^t show a dramatic spike feature whereas U_3^t exhibits a sharp dip, instead of the step-like jumps in 4L/2L CrI_3. Second, between B_{c1} and B_{c2} ≈ 1.5 T, U_1^t increases gradually until the saturation at B_{c2} while U_3^t and U_4^t decreases slowly towards a finite intensity and zero, respectively, rather than the plateaus of constant intensities in 4L/2L CrI_3. These two clear discrepancies between the magnetic field dependencies of the 1.1° tDB and 4L/2L CrI_3 strongly suggest the emergence of a fundamentally new magnetic phase in the tDB CrI_3 of intermediate twist angles, and therefore the distinction from magnetism in both small and large twist angle tDB CrI_3.

The anomalous behaviors of the 1.1° tDB CrI_3 above are further supported by the observation of large Raman circular dichroism at 0 T which is absolutely zero in 4L and 2L CrI_3 [38]. Figures 4a and 4b show the raw spectra of the 1.1° tDB CrI_3 taken at 0 T in both the LL and RR channels and their corresponding Lorentzian fitting profiles for individual modes, where LL (RR) refers to the incident and scattered light with left- (right-) handed circular polarizations. Here, we note that we could only resolve three ($U^t_{1,3,4}$) out of the four Raman modes because U^t_2 is overwhelmed by the spectrally closest and much stronger U^t_1 in the same co-circularly polarized channels. Clearly, U^t_1 and U^t_3 show substantial differences between the LL and RR channels with opposite relative intensities, whereas U^t_4 is almost helicity independent. Figure 4c presents the $B_\perp$ dependencies of the fitted intensities of $U^t_{1,3,4}$ in both co-circularly polarized channels, where the field is swept from + 2 T to – 2 T and then back to + 2 T. The two key features highlighted in Fig. 3h, the sharp dip/peak around B_{c1} for U^t_3/U^t_4 and the gradual evolution between B_{c1} and B_{c2} for all modes, are nicely reproduced in Fig. 4c. In addition, a third feature noticed is that U^t_1 and U^t_3 exhibit notable hysteresis loops below B_{c1}, in consistency with their substantial Raman circular dichroism even at 0 T.

Let us point out two important facts before establishing the understanding on these three key features in the 1.1° tDB CrI_3. First, recent DFT calculations show that both monoclinic and rhombohedral stackings between layers are structurally favorable with nearly identical elastic energies, yet they correspond to distinct interlayer AFM and FM exchange coupling, respectively [37]. In a moiré supercell of the 1.1° tDB CrI_3, both monoclinic and rhombohedral stacking regions take up appreciable amount of areas and feature the strong but opposite magnetic coupling across the 2L-2L interface, leading to the competition and frustration of spins at the boundaries between the monoclinic and rhombohedral stacking regions. Second, our polar magneto-Raman geometry is only sensitive to the out-of-plane components of spins. Although our probe and analysis do not directly account for the in-plane components of spins which are likely to develop from the aforementioned frustrations [3,4], our results on the out-of-plane magnetic orders in tDB CrI_3, at the same time, are compatible with the presence of in-plane spin components.

Therefore, we propose the following model for the magnetism in the 1.1° tDB CrI_3, where the strongly coupled 2L-2L regions have two types, the monoclinic AFM and the rhombohedral FM inter-2L coupling, and the optimized out-of-plane magnetic order features ↑↓↑↓ for the monoclinic regions and ↑↑↑↓ for the rhombohedral regions. As shown in Supplemental Information S1, based on parameters obtained from DFT calculations, this spin configuration has the lowest magnetic energy for intermediate twist angles. Because the ↑↑↑↓ state generates a net magnetization and contributes an effective out-of-plane magnetic field, which causes the re-orientation of the spins in the outermost layer to require a lower external $B_\perp$ in the rhombohedral regions than that in the monoclinic regions, i.e., $B^R_{c1} < B^M_{c1}$ with R(M) denoting the rhombohedral(monoclinic) stacking. Therefore, as a function of $B_\perp$, the magnetic state of the 1.1° tDB CrI_3

undergoes three critical transitions at B_{c1}^{R} = 0.5 T, B_{c1}^{M} = 0.7 T, and B_{c2} = 1.5 T, corresponding to the spin reorientation in the outermost layer in the rhombohedral and monoclinic regions, and the interior layer in the monoclinic regions, as depicted in Fig. 4d. We now can understand the three key features in the 1.1° tDB CrI_3. First, the dip/peak around 0.6 T for U_3^t/U_4^t in fact corresponds to the narrow field range between B_{c1}^{R} and B_{c1}^{M}, where the spin state of ↑↑↑↑ in the rhombohedral regions provides the least magnetism-coupled phonon contribution for $U_{3,4}^t$ modes (see Supplemental Information S2). Second, the gradual $B_\perp$ dependencies of all modes between B_{c1}^{M} and B_{c2} are then due to spin flop towards the $B_\perp$ direction, either by the expansion of the polarized area or by the increase in the out-of-plane components. Third, the Raman circular dichroism of $U_{1,3}^t$ at 0 T is from the interference between the individual pure structural and magnetism-coupled phonon contributions both of which are present for the ↑↑↑↓ state in the rhombohedral regions at 0 T. Thus, the hysteresis of $U_{1,3}^t$ below B_{c1}^{R} is naturally explained.

In summary, we have successfully engineered the 2D magnetism in tDB CrI_3 that exhibits a clear twist angle dependence. Although different from that of 4L/2L CrI_3, the magnetism in the very small and large twist angle tDB CrI_3 are dominated by the superpositions between 4L- and 2L-like regions, whereas that in the intermediate twist angle features fundamentally new magnetic orders that are absent in 4L/2L CrI_3. Our results open up experimental pathways for engineering and understanding 2D moiré magnetism, among which we highlight two immediate opportunities. One is the exploitation of in-plane spin component sensitive experimental techniques, for example, nonlinear optical spectroscopy [43-45], to develop a comprehensive understanding of moiré magnets where noncollinear spin textures with in-plane components often happen. The other is the exploration of moiré magnets for which the interlayer exchange coupling dominates over the intralayer exchange isotropy in the composing 2D magnets, such as 2D XY-type magnets [46,47], so that the periodic moiré interlayer exchange interaction is the leading order magnetic energy scale.

Methods

Growth of CrI_3 single crystals Single crystals of CrI_3 were grown by the chemical vapor transport method. Chromium power (99.99% purity) and iodine flakes (99.999% purity) in a 1:3 molar ratio were put into a silicon tube with a length of 200 mm and an inner diameter of 14 mm. The tube was pumped down to 0.01 Pa and sealed under vacuum, and then placed in a two-zone horizontal tube furnace whose two zones were raised up slowly to 903 K and 823 K for 2 days and then held for another 7 days. Shiny, black, plate-like crystals with lateral dimensions of up to several millimeters were obtained from this growth procedure.

Fabrications of 2D CrI_3 and tDB CrI_3 Atomically thin 2D CrI_3 flakes were exfoliated in a nitrogen-filled glovebox, and their thickness was first determined by the optical color contrast to select natural 4L and 2L CrI_3 and further confirmed using Raman spectroscopy at 10 K. Using a polymer-stamping technique inside the glovebox, large-size (lateral dimensions greater than 10 μm) 2L CrI_3 flakes were torn into two parts with similar sizes, one of which was rotated by a well-controlled rotation micrometer for targeted twist angles and then brought down to stack with the remaining half. Both 4L/2L and tDB CrI_3 samples were sandwiched between two few-layer hBN flakes to avoid surface reactions with oxygen and moisture in the ambient environment after taking out from the glovebox. The samples for magneto-Raman spectroscopy measurements were placed onto the SiO_2/Si substrate, and those for TEM measurements were transferred onto to TEM grids.

Micro-Raman spectroscopy Micro-Raman spectroscopy measurements were carried out using a 632.81 nm excitation laser with a full width half maximum (FWHM) of 0.85 cm^{-1}, on the resonance with the charge transfer and Cr^{3+} $^4A_2$ to $^4A_1$ transitions of CrI_3 in order to increase the Raman sensitivity. The laser beam on the sample site was focused down to ~ 3 μm FWHM in diameter using a 40× transmissive objective, and the laser power was kept at about 80 μW, in order to minimize the local heating effect during measurements. Backscattering geometry was used, where the scattered light was dispersed by a Horiba LabRAM HR Evolution Raman microscope (1800 grooves/mm grating) from Horiba Scientific and detected by a thermoelectric cooled CCD camera from Horiba Scientific. A commercial variable temperature (< 10 K – 325 K), closed cycle, microscopy cryostat from Cryo Industries of America, Inc was interfaced with the Raman microscope. A commercial cryogen free room-temperature-bore (2'' in diameter and 6.88'' long) superconducting magnet from Cryo Industries of America, Inc was used to achieve the variable out-of-plane magnetic field from 0 T to 2 T. The cryostat cold finger, on which the samples were mounted, was inserted into the center of the room-temperature-bore of the magnet. The linearly polarized magnto-Raman measurements were calibrated by suppressing the Rayleigh line in the linearly crossed channel, so as to overcome the Faraday artifact that is caused by the stray magnetic fields passing through

the objective. The circularly polarized magneto-Raman measurements were not affected by this Faraday effect, and therefore no corrections were applied.

Transmission Electron Microscopy Crystallographic orientations of the two composing 2L CrI_3 flakes in a tDB CrI_3 homostructure were identified by selected area electron diffraction measurements on Thermo Fisher Talos operated at 200 keV, equipped with Gatan OneView camera. Each Bragg peak was fitted with a 2D Gaussian to quantify the twist angle in reciprocal space. A total of nine locations were surveyed for the homostructure to develop a statistical confidence in assigning the twist angle and its standard deviation. Figure 1c was generated by averaging DF-TEM images from three 5^{th} order Bragg peaks, spaced 120° apart to remove anisotropy.

Data availability

The datasets generated and/or analyzed during the current study are available from the corresponding authors on reasonable request.

Acknowledgement

L. Zhao acknowledges the support by NSF CAREER Grant No. DMR-174774 and AFOSR YIP Grant No. FA9550-21-1-0065. R. He acknowledges the support by NSF CAREER Grant No. DMR-1760668. K. Sun acknowledges the support by NSF Grant No. NSF-EFMA-1741618. R. Hovden acknowledges the support from W. M. Keck Foundation. This work made use of facilities at Michigan Center for Materials Characterization. H. Lei acknowledges support by the National Key R&D Program of China (Grant No. 2018YFE0202600, 2016YFA0300504), the National Natural Science Foundation of China (No. 11774423, and 11822412), the Beijing Natural Science Foundation (Grant No. Z200005), and the Fundamental Research Funds for the Central Universities and Research Funds of Renmin University of China (RUC) (Grant No. 18XNLG14 and 19XNLG17, 20XNH062).

Author contributions

L. Zhao, H. Xie, and X. Luo conceived the ideal and initiated this project; H. Xie fabricated the 4L and 2L CrI_3 and tDB CrI_3 homostructures; H. Xie, X. Luo, G. Ye, Z. Ye, and H. Ge carried out the Raman experiments under the supervision of L. Zhao and R. He; S. H. Sung, E. Rennich, and R. Hovden performed the TEM characterizations; S. Yan, Y. Fu, S. Tian, and H. Lei grew the vdW CrI_3 bulk single crystals; K.

Sun performed the theoretical calculations; H. Xie, X. Luo, R. He, and L. Zhao analyzed the data and wrote the manuscript; all authors participated in the discussion of the results.

Competing interests

The authors declare no competing interests.

Figure captions

Figure 1. Sample fabrication, TEM and magneto-Raman characterizations of tDB CrI_3. a. False-colored optical images for a tDB CrI_3 homostructure (top panel) with two composing 2L CrI_3 outlined with red lines and its original large-size 2L CrI_3 (bottom panel) with the tearing boundary marked with a white dashed line. **b.** Electron diffraction patterns of 1st and 2nd order Bragg peaks for a tDB CrI_3 with a targeted twist angle α of 1.0°, showing the measured value of α = 0.9° ± 0.1° based on the survey over nine areas in this tDB CrI_3. **c.** Averaged DF-TEM real space image from three 5th order Bragg peaks showing the hexagonal superlattice network in the 0.9° tDB CrI_3 in **b**. **d.** Full-range Raman spectra taken on a 1.1° tDB CrI_3 sample in both the crossed (blue) and parallel (gray) linear polarization channels at 10 K. The parallel channel spectrum is scaled by a factor of 0.33 for a better visual comparison with the crossed channel one. **e.** Zoom-in of Raman spectra over the 120 – 133 cm^{-1} frequency range taken on the same 1.1° tDB CrI_3 sample as in **d** in both the parallel (blue) and crossed (gray) channels at two incident polarizations of θ_{inc} = 0° (filled circles and solid lines) and 45° (open circles and dashed lines) at 10 K. The parallel channel spectra are scaled by a factor of 0.33.

Figure 2. Twist angle dependence of the magneto-Raman spectra of tDB CrI_3. a. Raman spectra taken on 4L CrI_3, tDB CrI_3 homostructures with targeted twist angles of α = 0.5°, 1.1°, 2.0°, and 5.0°, and 2L CrI_3 in both the crossed (blue dots and lines) and parallel (gray) channels at 10 K. The Raman spectra are scaled by factors labeled in individual panels. The Raman modes are also marked at their corresponding frequencies, with $U^{4L}_{1,2,3,4}$, $U^{t}_{1,2,3,4}$, and $U^{2L}_{1,2}$ for 4L, tDB, and 2L CrI_3. The colored Lorentzian profiles highlight individual modes appearing in the crossed channel, with red (blue) for the central (two side) mode(s) in the triplet spectra of tDB CrI_3 and the mode(s) of 2L (4L) CrI_3. **b.** Plot of the fitted Raman frequencies of individual modes in every spectrum shown in **a** as a function of the twist angle. **c.** Plot of the

intensity ratio $I_{U_3^t}/(I_{U_2^t}+I_{U_4^t})$ as a function of the twist angle. Error bars correspond to one standard error in fitting the Raman spectra.

Figure 3. Magnetic field dependence of the magneto-Raman spectra of tDB CrI_3 at selected twist angles. a-e. False-colored maps of the $B_\perp$ dependent Raman spectra taken on 4L CrI_3, tDB CrI_3 homostructures with targeted twist angles α = 0.5°, 1.1°, and 5.0°, and 2L CrI_3, respectively, in the crossed linear polarization channel at 10 K. The blue arrows mark the frequencies of $U_{1,2,3,4}^{4L}$ for 4L CrI_3, and the red ones are for those of $U_{1,2}^{2L}$ for 2L CrI_3. **f-j.** Plots of the fitted mode intensities as a function of $B_\perp$ for the samples in **a-e**. Open squares are for the fitted values. Thin black lines and solid shaded areas are for the fits to the established model of the magnetism-coupled phonon scattering for the 4L (**f**) and 2L (**j**) CrI_3, and to the proposed weighted linear superpositions of 4L and 2L contributions for the very small (0.5°, **g**) and large (5.0°, **j**) twist angle tDB CrI_3. Thick gray lines and the striped areas in **h** are guide to the eye. Error bars correspond to one standard error in fitting the Raman spectra.

Figure 4. Magnetic circular dichroism for the 1.1° twist angle tDB CrI_3. a. Raman spectra taken in the LL (red) and RR (blue) co-circularly polarized channels at 10 K on the 1.1° tDB CrI_3. **b.** Fitted Lorentzian profiles for individual modes ($U_{1,3,4}^t$) in the Raman spectra in **a**. **c.** Plots of fitted mode intensities for $U_{1,3,4}^t$ as a function of $B_\perp$ that is swept from + 2 T to – 2 T (decreasing B, open circle/square for the LL/RR channel) and then to + 2 T (increasing B, solid circle/square for the LL/RR channel). Three critical magnetic fields, B_{c1}^R, B_{c1}^M, and B_{c2}, are marked on both the upwards and downwards magnetic fields, and four magnetic field ranges, below B_{c1}^R, B_{c1}^R to B_{c1}^M, B_{c1}^M to B_{c2}, and above B_{c2} are shaded, respectively, with light green, orange, blue, and red. **d.** Sketches of the out-of-plane layered magnetism in the two types of strongly coupled 2L-2L regions of a moiré supercell, monoclinic (M) and rhombohedral (R) ones, evolving as the $B_\perp$ increases across B_{c1}^R, B_{c1}^M, and B_{c2}.

References

1 Balents, L., Dean, C. R., Efetov, D. K. & Young, A. F. Superconductivity and strong correlations in moiré flat bands. *Nature Physics* **16**, 725-733, doi:10.1038/s41567-020-0906-9 (2020).

2 Kennes, D. M. *et al.* Moiré heterostructures as a condensed-matter quantum simulator. *Nature Physics* **17**, 155-163, doi:10.1038/s41567-020-01154-3 (2021).

3 Hejazi, K., Luo, Z.-X. & Balents, L. Noncollinear phases in moiré magnets. *Proceedings of the National Academy of Sciences* **117**, 10721, doi:10.1073/pnas.2000347117 (2020).

4 Tong, Q., Liu, F., Xiao, J. & Yao, W. Skyrmions in the Moiré of van der Waals 2D Magnets. *Nano Letters* **18**, 7194-7199, doi:10.1021/acs.nanolett.8b03315 (2018).
5 Wang, C., Gao, Y., Lv, H., Xu, X. & Xiao, D. Stacking Domain Wall Magnons in Twisted van der Waals Magnets. *Physical Review Letters* **125**, 247201, doi:10.1103/PhysRevLett.125.247201 (2020).
6 Cao, Y. *et al.* Correlated insulator behaviour at half-filling in magic-angle graphene superlattices. *Nature* **556**, 80-84, doi:10.1038/nature26154 (2018).
7 Cao, Y. *et al.* Unconventional superconductivity in magic-angle graphene superlattices. *Nature* **556**, 43-50, doi:10.1038/nature26160 (2018).
8 Regan, E. C. *et al.* Mott and generalized Wigner crystal states in WSe_2/WS_2 moiré superlattices. *Nature* **579**, 359-363, doi:10.1038/s41586-020-2092-4 (2020).
9 Tang, Y. *et al.* Simulation of Hubbard model physics in WSe_2/WS_2 moiré superlattices. *Nature* **579**, 353-358, doi:10.1038/s41586-020-2085-3 (2020).
10 Kim, K. *et al.* Tunable moiré bands and strong correlations in small-twist-angle bilayer graphene. *Proceedings of the National Academy of Sciences* **114**, 3364, doi:10.1073/pnas.1620140114 (2017).
11 Nuckolls, K. P. *et al.* Strongly correlated Chern insulators in magic-angle twisted bilayer graphene. *Nature* **588**, 610-615, doi:10.1038/s41586-020-3028-8 (2020).
12 Wu, S., Zhang, Z., Watanabe, K., Taniguchi, T. & Andrei, E. Y. Chern insulators, van Hove singularities and topological flat bands in magic-angle twisted bilayer graphene. *Nature Materials*, doi:10.1038/s41563-020-00911-2 (2021).
13 Chen, G. *et al.* Tunable correlated Chern insulator and ferromagnetism in a moiré superlattice. *Nature* **579**, 56-61, doi:10.1038/s41586-020-2049-7 (2020).
14 Tran, K. *et al.* Evidence for moiré excitons in van der Waals heterostructures. *Nature* **567**, 71-75, doi:10.1038/s41586-019-0975-z (2019).
15 Jin, C. *et al.* Observation of moiré excitons in WSe_2/WS_2 heterostructure superlattices. *Nature* **567**, 76-80, doi:10.1038/s41586-019-0976-y (2019).
16 Wang, J. *et al.* Optical generation of high carrier densities in 2D semiconductor heterobilayers. *Science Advances* **5**, eaax0145, doi:10.1126/sciadv.aax0145 (2019).
17 Seyler, K. L. *et al.* Signatures of moiré-trapped valley excitons in $MoSe_2/WSe_2$ heterobilayers. *Nature* **567**, 66-70, doi:10.1038/s41586-019-0957-1 (2019).
18 Yoo, H. *et al.* Atomic and electronic reconstruction at the van der Waals interface in twisted bilayer graphene. *Nature Materials* **18**, 448-453, doi:10.1038/s41563-019-0346-z (2019).
19 Alden, J. S. *et al.* Strain solitons and topological defects in bilayer graphene. *Proceedings of the National Academy of Sciences*, 201309394, doi:10.1073/pnas.1309394110 (2013).
20 Quan, J. *et al.* Phonon renormalization in reconstructed MoS_2 moiré superlattices. *Nature Materials*, doi:10.1038/s41563-021-00960-1 (2021).
21 Lin, M.-L. *et al.* Moiré Phonons in Twisted Bilayer MoS_2. *ACS Nano* **12**, 8770-8780, doi:10.1021/acsnano.8b05006 (2018).
22 Burch, K. S., Mandrus, D. & Park, J.-G. Magnetism in two-dimensional van der Waals materials. *Nature* **563**, 47-52, doi:10.1038/s41586-018-0631-z (2018).
23 Gong, C. & Zhang, X. Two-dimensional magnetic crystals and emergent heterostructure devices. *Science* **363**, eaav4450, doi:10.1126/science.aav4450 (2019).
24 Mak, K. F., Shan, J. & Ralph, D. C. Probing and controlling magnetic states in 2D layered magnetic materials. *Nature Reviews Physics* **1**, 646-661, doi:10.1038/s42254-019-0110-y (2019).
25 Huang, B. *et al.* Layer-dependent ferromagnetism in a van der Waals crystal down to the monolayer limit. *Nature* **546**, 270-273, doi:10.1038/nature22391 (2017).
26 Wang, Z. *et al.* Determining the phase diagram of atomically thin layered antiferromagnet $CrCl_3$. *Nature Nanotechnology* **14**, 1116-1122, doi:10.1038/s41565-019-0565-0 (2019).
27 Chen, W. *et al.* Direct observation of van der Waals stacking–dependent interlayer magnetism. *Science* **366**, 983, doi:10.1126/science.aav1937 (2019).

28 Kim, H. H. *et al.* Evolution of interlayer and intralayer magnetism in three atomically thin chromium trihalides. *Proceedings of the National Academy of Sciences* **116**, 11131, doi:10.1073/pnas.1902100116 (2019).

29 Klein, D. R. *et al.* Probing magnetism in 2D van der Waals crystalline insulators via electron tunneling. *Science* **360**, 1218, doi:10.1126/science.aar3617 (2018).

30 Jin, W. *et al.* Observation of the polaronic character of excitons in a two-dimensional semiconducting magnet CrI_3. *Nature Communications* **11**, 4780, doi:10.1038/s41467-020-18627-x (2020).

31 Li, S. *et al.* Magnetic-Field-Induced Quantum Phase Transitions in a van der Waals Magnet. *Physical Review X* **10**, 011075, doi:10.1103/PhysRevX.10.011075 (2020).

32 Jiang, S., Li, L., Wang, Z., Mak, K. F. & Shan, J. Controlling magnetism in 2D CrI_3 by electrostatic doping. *Nature Nanotechnology* **13**, 549-553, doi:10.1038/s41565-018-0135-x (2018).

33 Huang, B. *et al.* Electrical control of 2D magnetism in bilayer CrI_3. *Nature Nanotechnology* **13**, 544-548, doi:10.1038/s41565-018-0121-3 (2018).

34 Jiang, S., Shan, J. & Mak, K. F. Electric-field switching of two-dimensional van der Waals magnets. *Nature Materials* **17**, 406-410, doi:10.1038/s41563-018-0040-6 (2018).

35 Li, T. *et al.* Pressure-controlled interlayer magnetism in atomically thin CrI_3. *Nature Materials* **18**, 1303-1308, doi:10.1038/s41563-019-0506-1 (2019).

36 Song, T. *et al.* Switching 2D magnetic states via pressure tuning of layer stacking. *Nature Materials* **18**, 1298-1302, doi:10.1038/s41563-019-0505-2 (2019).

37 Sivadas, N., Okamoto, S., Xu, X., Fennie, C. J. & Xiao, D. Stacking-Dependent Magnetism in Bilayer CrI_3. *Nano Letters* **18**, 7658-7664, doi:10.1021/acs.nanolett.8b03321 (2018).

38 Jin, W. *et al.* Tunable layered-magnetism–assisted magneto-Raman effect in a two-dimensional magnet CrI_3. *Proceedings of the National Academy of Sciences* **117**, 24664, doi:10.1073/pnas.2012980117 (2020).

39 Jin, W. *et al.* Raman fingerprint of two terahertz spin wave branches in a two-dimensional honeycomb Ising ferromagnet. *Nature Communications* **9**, 5122, doi:10.1038/s41467-018-07547-6 (2018).

40 Huang, B. *et al.* Tuning inelastic light scattering via symmetry control in the two-dimensional magnet CrI_3. *Nature Nanotechnology* **15**, 212-216, doi:10.1038/s41565-019-0598-4 (2020).

41 Zhang, Y. *et al.* Magnetic Order-Induced Polarization Anomaly of Raman Scattering in 2D Magnet CrI_3. *Nano Letters* **20**, 729-734, doi:10.1021/acs.nanolett.9b04634 (2020).

42 McCreary, A. *et al.* Distinct magneto-Raman signatures of spin-flip phase transitions in CrI_3. *Nature Communications* **11**, 3879, doi:10.1038/s41467-020-17320-3 (2020).

43 Zhao, L. *et al.* Evidence of an odd-parity hidden order in a spin–orbit coupled correlated iridate. *Nature Physics* **12**, 32-36, doi:10.1038/nphys3517 (2016).

44 Zhao, L. *et al.* A global inversion-symmetry-broken phase inside the pseudogap region of $YBa_2Cu_3O_y$. *Nature Physics* **13**, 250-254, doi:10.1038/nphys3962 (2017).

45 Jin, W. *et al.* Observation of a ferro-rotational order coupled with second-order nonlinear optical fields. *Nature Physics* **16**, 42-46, doi:10.1038/s41567-019-0695-1 (2020).

46 Kim, K. *et al.* Suppression of magnetic ordering in XXZ-type antiferromagnetic monolayer $NiPS_3$. *Nature Communications* **10**, 345, doi:10.1038/s41467-018-08284-6 (2019).

47 Bedoya-Pinto, A. *et al.* Intrinsic 2D-XY ferromagnetism in a van der Waals monolayer. *arXiv preprint arXiv:2006.07605* (2020).

Figures

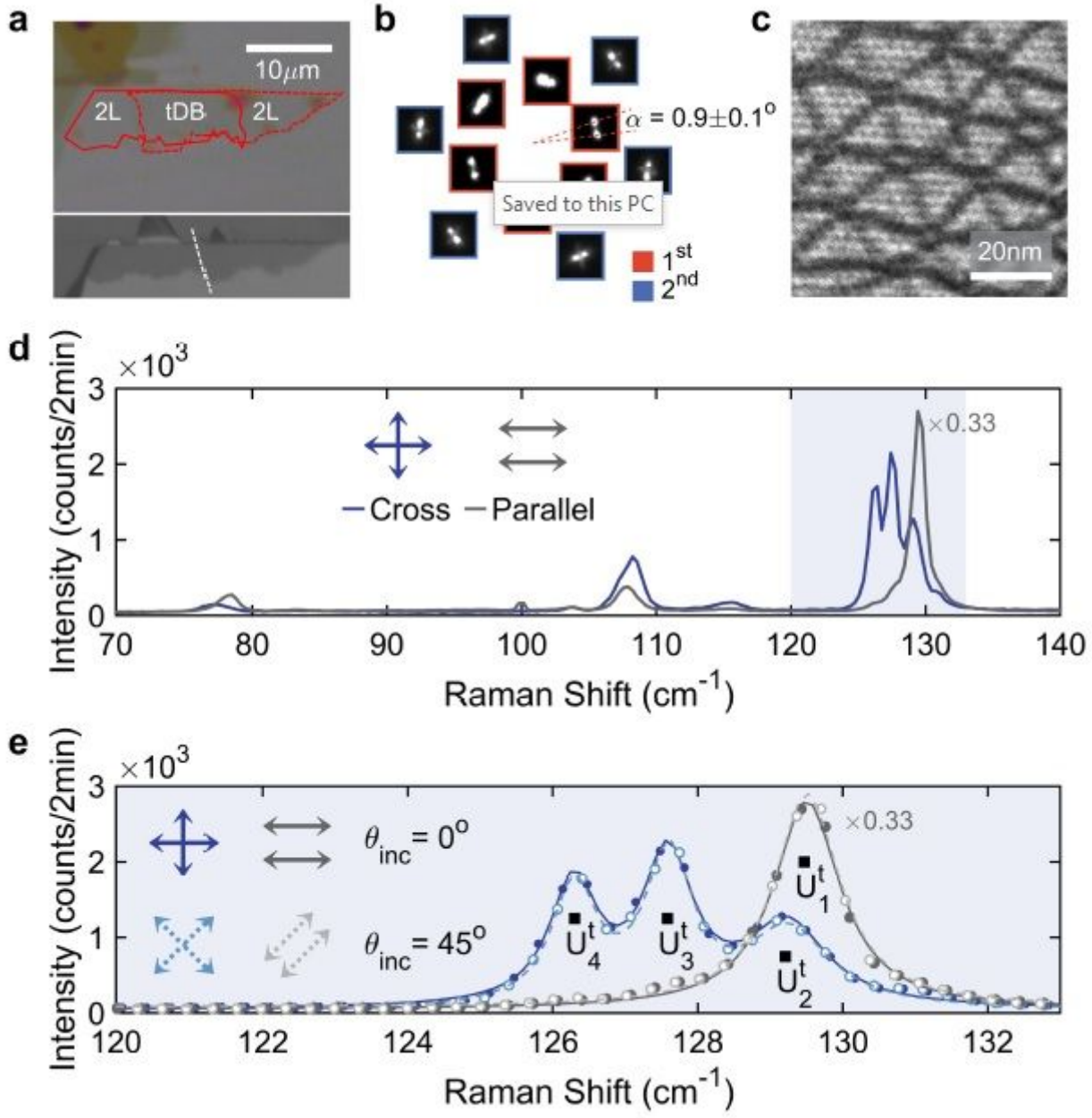

Figure 1

Sample fabrication, TEM and magneto-Raman characterizations of tDB CrI3. (see Manuscript file for full figure legend)

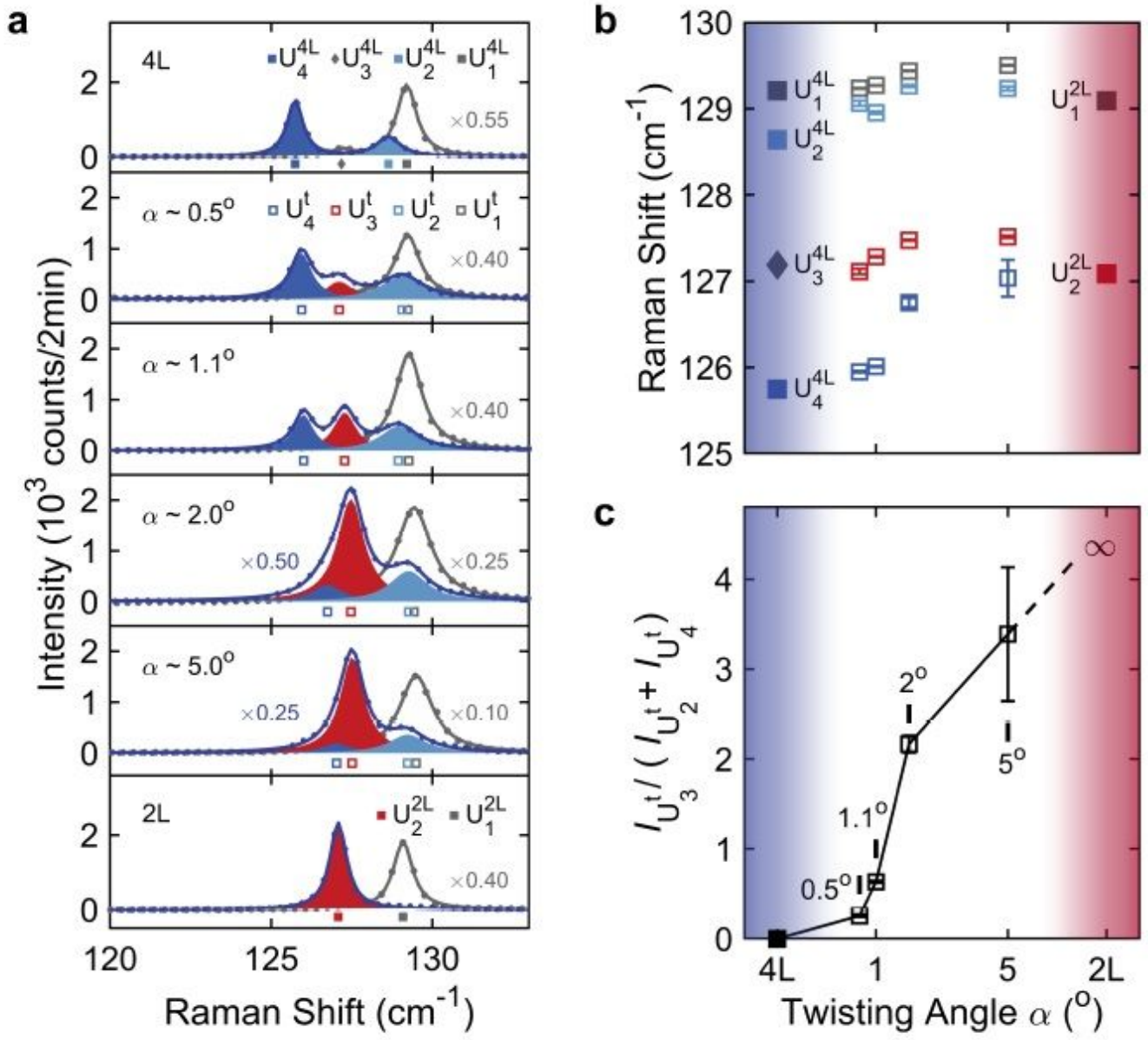

Figure 2

Twist angle dependence of the magneto-Raman spectra of tDB CrI3. (see Manuscript file for full figure legend)

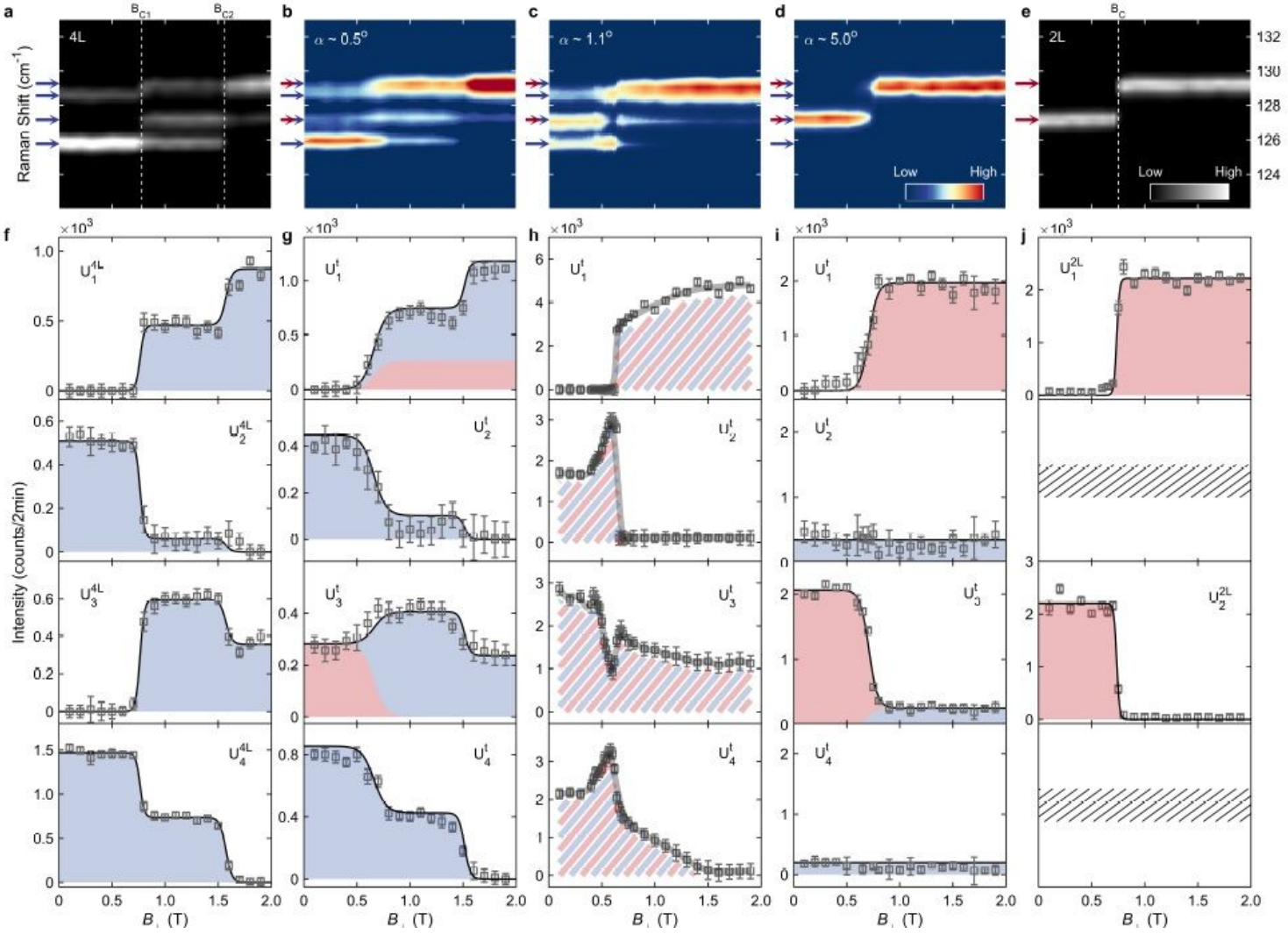

Figure 3

Magnetic field dependence of the magneto-Raman spectra of tDB CrI3 at selected twist angles. (see Manuscript file for full figure legend)

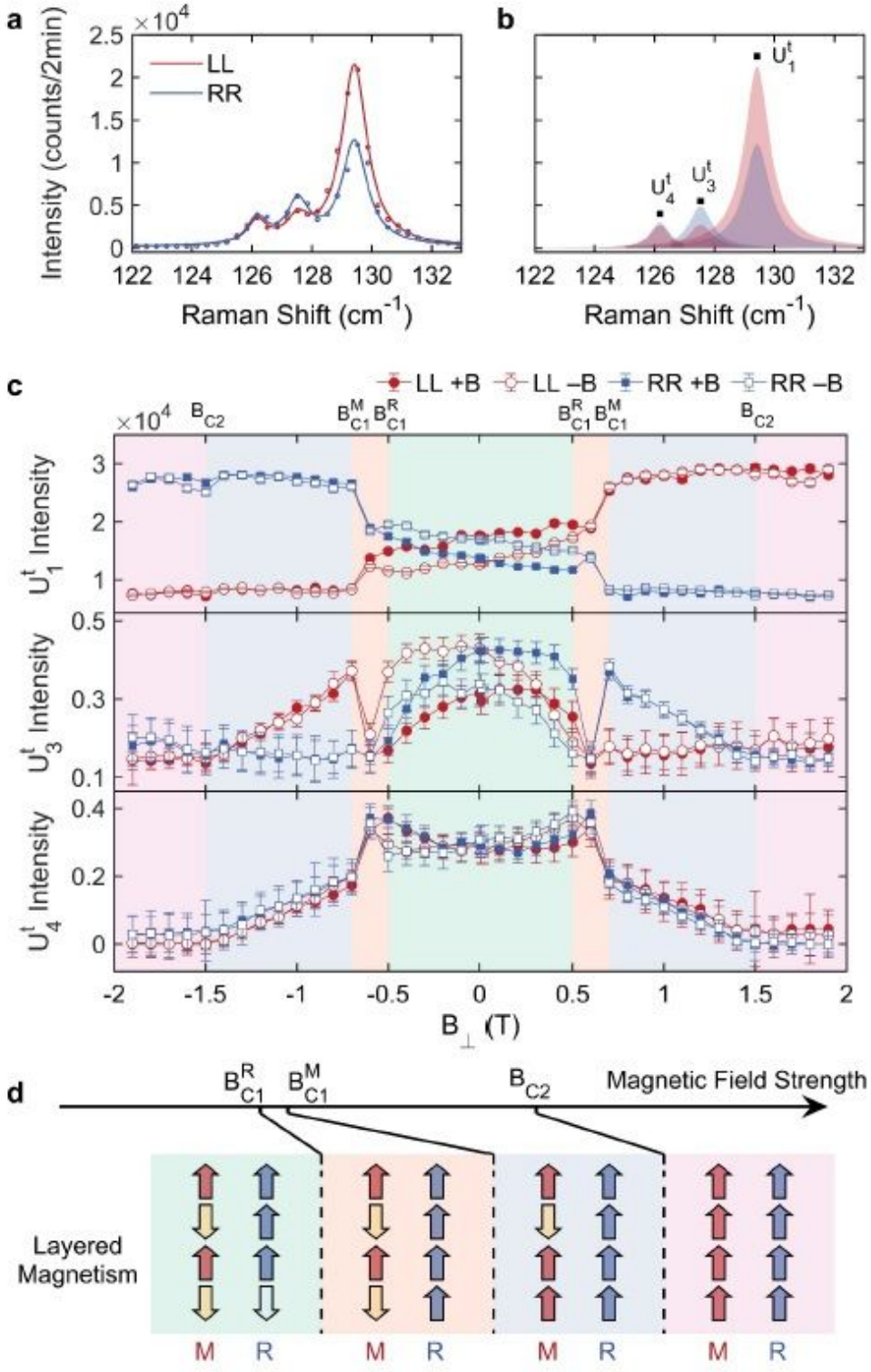

Figure 4

Magnetic circular dichroism for the 1.1o twist angle tDB CrI3. (see Manuscript file for full figure legend)

Supplementary Files

This is a list of supplementary files associated with this preprint. Click to download.

- SupplementalInformation.pdf